Oxygen Deficient Interfacial Effect in CeO_2-Modified Fe_2O_3/C for Oxygen Reduction Reaction in Alkaline Electrolyte*

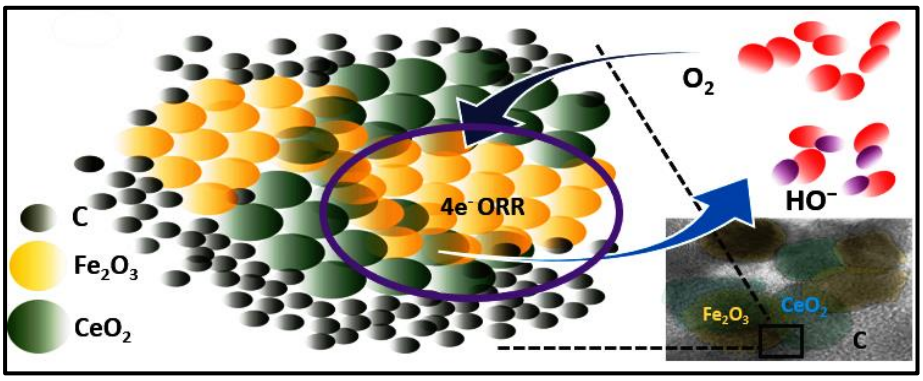

A facile two-step solvothermal synthesis of a heterostructure of Fe_2O_3-CeO_2/C for oxygen reduction electrocatalysis is discussed in this chapter. The EC possessed large surface oxygen vacancies, massive oxide-oxide and oxide-carbon interfaces, as revealed from XPS, Raman and TEM results. A study with various electrochemical studies exhibited by Fe_2O_3-CeO_2/C establishes that it acts as a high-performance, durable and stable EC toward ORR in alkaline electrolyte. To investigate the promotional and synergistic effects of CeO_2 on Fe_2O_3-CeO_2/C, the individual parent ECs i.e., Fe_2O_3/C and CeO_2/C were synthesized and studied their electrocatalytic actions toward ORR. Moreover, the effect of excessive or insufficient Fe_2O_3 in Fe_2O_3-CeO_2/C heterostructure for ORR electrocatalysis is discussed in this chapter. All the experimental methodologies for the synthesis, physicochemical and electrochemical characterization used in this chapter were discussed in Chapter 2.

*The content of this chapter has been published in " *Catalysis Communications,* 164: 106432, 2022"

5.1. Introduction

The ever-increasing global energy demands have accelerated substantial strategies for the development of efficient, cost-effective, and eco-friendly energy storage and conversion systems [1–4]. An efficient ORR on the cathode surface is crucially significant for the new generation energy storage and conversion devices. As the sluggish kinetics at the cathode surface perpetually hinder the efficiency of ORR; a suitable electrocatalytic surface is intensely recommended to achieve the desired activity [5]. ECs are the key component of major renewable-energy technologies such as fuel cells, metal-air batteries, and water splitting. Pt-based materials are observed to be the most active ECs for ORR due to their intrinsic catalytic properties [6,7]. Nevertheless, the high cost and lack of stability in both acidic and alkaline media still restrict Pt-based ECs for effective commercialization. Transition metal oxide/carbon (TMO/C) composite has been extensively investigated in recent times because of its low cost, easy availability, and high activity toward ORR [8–10]. The high electrical conductivity of C facilitates electron transfer and enhances the electrocatalytic activity of the ORR process. TMO/C (M_xO_y/C; M= Mn, Fe, Co, Ni, Cu etc) composite enhances the surface electrical conductivity rendering abundant catalytically active sites. CeO_2-modified TMO/C materials possess characteristic properties exhibiting more efficient ORR because of the unique redox nature of CeO_2 [2,7,8]. Cerium in CeO_2 exists in Ce(III/IV) state because of the inherent lattice defect, availing sort of oxygen vacancies. Consequently, CeO_2 act as an oxygen buffer and enhances the rate of O_2 adsorption/desorption during the ORR process [8,13,14]. Taking all such aspects into consideration, we report the fabrication of Fe_2O_3-CeO_2/C nanocomposite with a rich interface structure as an efficient EC for ORR in alkaline electrolytes. The as-prepared Fe_2O_3-CeO_2/C exhibited superior ORR activity with excellent stability due to the enchantment of its unique intrinsic activity triggered by the synergistic action. This new composite material makes the best use of its intrinsic characteristics, resulting in a potential candidate for the next generation cathode ECs.

5.2. Results and Discussion

5.2.1. Characterization of the Fe_2O_3-CeO_2/C, Fe_2O_3/C and CeO_2/C ECs

PXRD patterns of the ECs, as sown in Figure 5.1. a. display the structural changes, crystallinity, and phase purity in Fe_2O_3-CeO_2/C. The broad and low-intensity

carbon (graphitic C-sp^2 structure) [15] peak at about 24° (2θ) vanishes in Fe_2O_3/C, Fe_2O_3-CeO_2/C and CeO_2/C because of the lower crystallinity of C. Fe_2O_3/C and CeO_2/C show the diffraction pattern of pure Fe_2O_3 (JCPDS No. 89-8104) and CeO_2 (JCPDS No. 81-0792) respectively, while Fe_2O_3-CeO_2/C shows discrete diffraction peaks of the both Fe_2O_3 and CeO_2 phases establishing extensive MO-MO interfaces. In addition, the peak intensity of the parent C, Fe_2O_3 and CeO_2 has significantly reduced in the mixed Fe_2O_3-CeO_2/C suggesting the formation of MO-MO/C interfaces. Raman spectroscopy analysis shows the effect of CeO_2 in Fe_2O_3/C as shown in Figure 5.1. b.

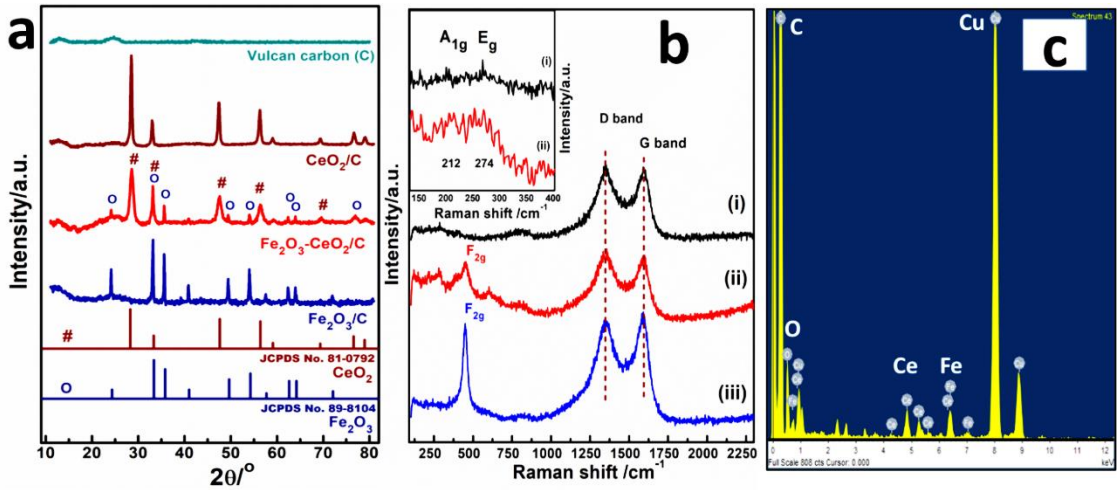

Figure 5.1. a) XRD patterns of C, CeO_2/C, Fe_2O_3-CeO_2/C and Fe_2O_3/C, b) Raman spectrum of Fe_2O_3/C (i), Fe_2O_3-CeO_2/C (ii) and CeO_2/C (iii) and c) EDX pattern of Fe_2O_3-CeO_2/C. (Cu peak observed in the EDX spectrum appear due to carbon-coated Cu grid used during the measurement.)

A sharp Raman peak at ~454 cm^{-1} is observed for CeO_2 which is attributed to the symmetric F_{2g} mode for *fcc* CeO_2 due to the symmetric O–Ce–O stretching over the surrounding oxygen atoms. However, the significant reduction of peak intensity and broadening of the F_{2g} peak in the Fe_2O_3-CeO_2/C infers the creation of more oxygen vacancy as the F_{2g} mode is highly labile to the disorder in the vicinity of oxygen sub-lattice [19]. Fe_2O_3/C exhibits two typical bands at 212 and 274 cm^{-1}, which are the characteristics Fe–O–Fe stretching of A_{1g} and E_g mode, respectively. The atomic percentage (At.%) in Fe_2O_3-CeO_2/C was accomplished by EDX as presented in Figure 5.1. c. The At.% of Fe, Ce, O and C in Fe_2O_3-CeO_2/C were 1, 1, 2 and 96 %, respectively. The percentage compositions of the associated ECs summarized in Table 5.1.

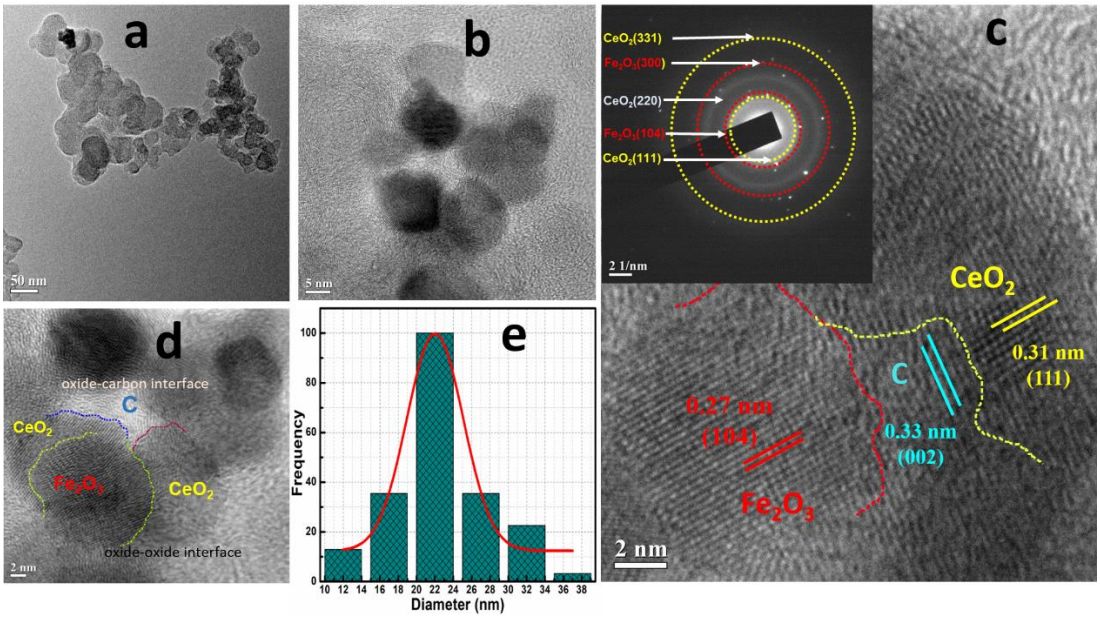

Figure 5.2. a-d) TEM and HRTEM images EC Fe_2O_3-CeO_2/C (inset of c shows the SAED pattern for the EC), and e) particle size distribution of Fe_2O_3-CeO_2/C.

To study the morphology of Fe_2O_3 and CeO_2 NPs aggregation in Fe_2O_3-CeO_2/C TEM analysis has been performed. Figure 5.2. a, b and d show the low-resolution TEM images of Fe_2O_3-CeO_2/C which reveal the homogeneous dispersion of Fe_2O_3 and CeO_2 over the C-matrix establishing massive interfaces randomly allocated at the microscopic dimension. The HR-TEM is shown in Figure 5.2. c further illustrates the overlapping regions of Fe_2O_3-CeO_2 over the C-matrix. The lattice spacing of about 0.27, 0.33 and 0.31 nm represent the typical Fe_2O_3 (104), C (002) and CeO_2 (111) crystal planes respectively [16–18]. The average particle size was observed to be ~22 nm (Figure 5.2. e). SAED pattern analysed for Fe_2O_3-CeO_2/C showed a set of diffraction rings due to the crystalline reflections of (111)-CeO_2, (104)-Fe_2O_3, (220)-CeO_2, (300)-Fe_2O_3 and (311)-CeO_2, as shown in the inset of Figure 5.2. c. which is well consistent with the XRD studies. The clear diffraction rings and the few additional bright spots nearby the diffraction rings suggest the polycrystalline and partial single crystalline nature of the investigated catalyst.

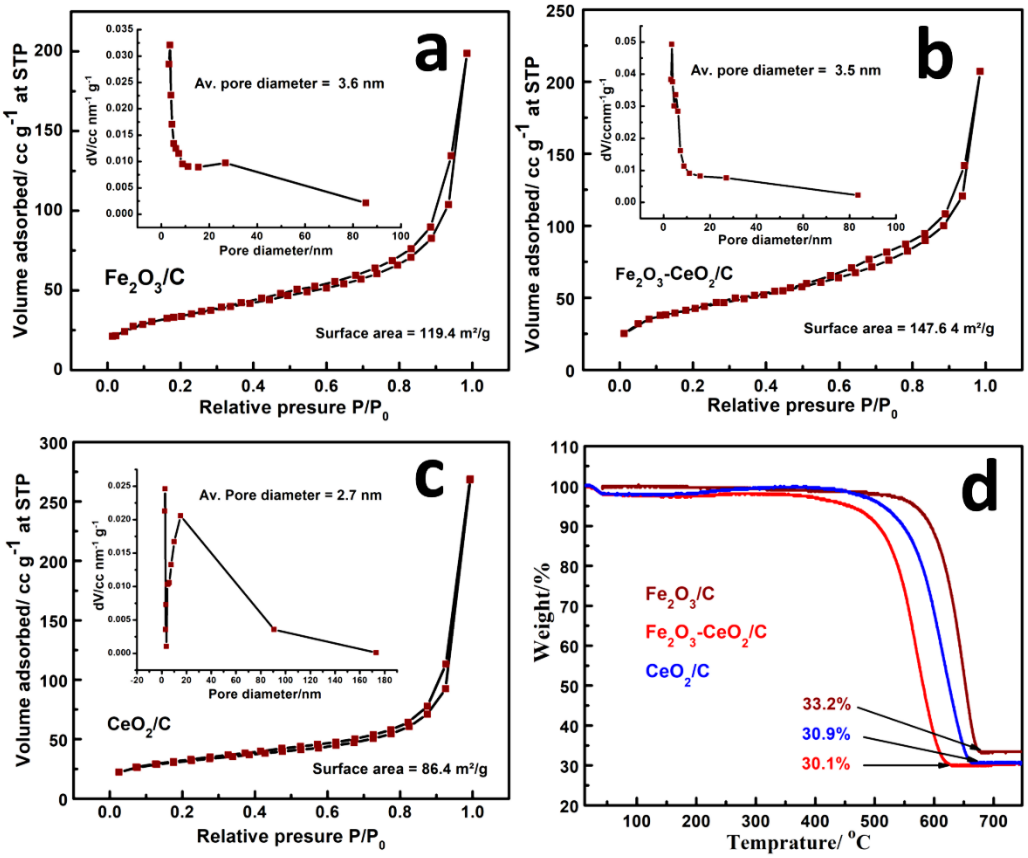

Figure 5.3. N_2 adsorption−desorption isotherms of (a) Fe_2O_3/C (b) Fe_2O_3-CeO_2/C and (c) CeO_2/C (inset shows the corresponding pore size distribution curve) and d) TGA profiles of Fe_2O_3/C, Fe_2O_3-CeO_2/C and CeO_2/C in air atmosphere.

The BET surface area of Fe_2O_3-CeO_2/C (147.6 m^2 g^{-1}) is higher than Fe_2O_3/C (119.4 m^2 g^{-1}) and CeO_2/C (86.4 m^2 g^{-1}) revealing that Fe_2O_3-CeO_2/C interfacial EC accommodates more active sites for the effective ORR (Figure 5.3. a-c). The evaluated average pore diameter is 3.6, 3.5 and 2.7 nm (insets of Figure 5.3. a-c), respectively for Fe_2O_3/C, Fe_2O_3-CeO_2/C and CeO_2/C, which specifies the mesoporous nature of the ECs. TGA analysis was carried out to determine the MO content of the ECs as presented in Figure 5.3. d. The TGA curves show ~70% weight loss at the temperature range of 550-600 ^oC which is due to the chemical dehydration, removal of counter ions and C oxidation. The remaining wt.% of ~30% are the MO content of the ECs.

Table 5.1. Textural properties of the as-prepared ECs.

ECs	Element	Wt. % [a]	At. % [a]	BET surface area (m^2/g)	Av. Pore size (nm)	ECSA (m^2/g)
Fe_2O_3/C	C	67.25	78.28	119.4	3.6	15
	O	21.67	18.94			
	Fe	11.09	2.78			
Fe_2O_3-CeO_2/C	C	70.02	82.64	147.6	3.5	20
	O	17.72	15.70			
	Fe	2.72	0.69			
	Ce	9.53	0.96			
CeO_2/C	C	71.54	79.73	86.4	2.7	35.9
	O	23.67	19.81			
	Ce	4.78	0.46			

[a] The Wt.% and At.% are evaluated based on EDX measurement.

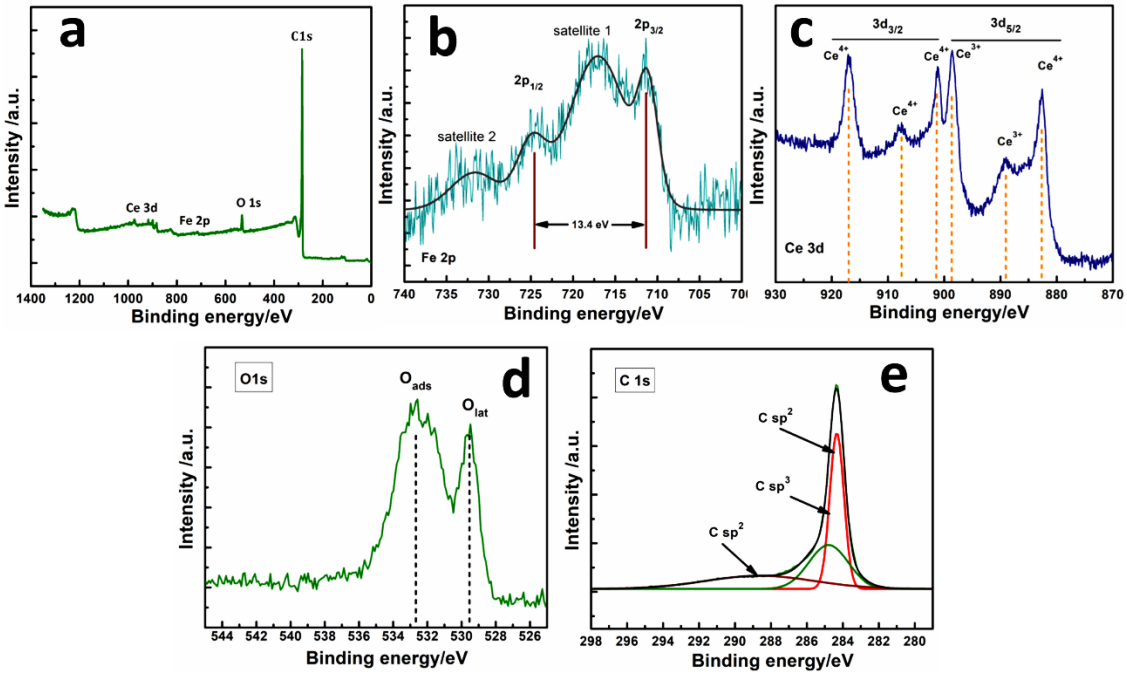

Figure 5.4. XPS spectra of Fe_2O_3-CeO_2/C EC: a) survey spectrum, b-e) core level XPS spectrum of Fe 2p, Ce 3d, O1s and C 1s, respectively.

The surface structures and the valence states of the ECs were further investigated by XPS analysis. The survey spectrum of Fe_2O_3-CeO_2/C reveals that Fe, Ce, O and C are the constituent elements of the EC (Figure 5.4. a). The Fe 2p spectrum

consists of two photoelectron peaks at BE of 711 eV for Fe $2p_{3/2}$ and 724.4 eV for $2p_{1/2}$ with Δ_{BE} = 13.4 eV and two intense broad satellite peaks (sat. 1 and sat. 2) originating from rapid change in Coulombic potential when the photoelectron passes through the valence band (Figure 5.4. b) [20]. The XPS spectrum of Ce 3d shows two sets of peaks, which can be assigned to $3d_{3/2}$ and $3d_{5/2}$ as shown in Figure 5.4. c. The peaks at 889 and 898.6 eV in the XPS spectrum are assigned to Ce^{3+} while the peaks at 882.6, 901.2, 907.5 and 916 eV are assigned to the Ce^{4+} state of cerium [21,22]. The Ce^{3+} content in CeO_2 is a typical descriptor of oxygen vacancy which determines the feasibility and enhancement of the $Ce^{4+} \leftrightarrow Ce^{3+}$ redox transition. The Ce 3d XPS result depicts that the Fe_2O_3-CeO_2/C is integrated with rich oxygen vacancies which are significant for efficient electrocatalytic ORR. The O 1s XPS spectrum is shown in Figure 5.4. d exhibit two distinct peaks for lattice oxygen (Fe-O, 529 eV), and surface adsorbed oxygen (532.6 eV) [23]. The deconvolution peaks of the C 1s spectrum display three peaks that could be assigned to sp^3-C and graphitic sp^2-C (Figure 5.4. e).

5.2.2. Electrocatalytic Activity towards ORR

Figure 5.5. a show the CV curves of the investigated ECs. The significant reduction peaks observed in the CVs under O_2 saturated 0.1M KOH solution suggest that the prepared ECs are active toward ORR. The ORR onset potential exhibited by C, Fe_2O_3/C and CeO_2/C is 0.75, 0.78 and 0.76 V (vs. RHE), respectively while for Fe_2O_3-CeO_2/C, it is observed to be 0.81 V, suggesting a significant overpotential drop for Fe_2O_3-CeO_2/C catalysed ORR process. Furthermore, it should be noted that as compared to C, CeO_2/C and Fe_2O_3/C, CeO_2 modified Fe_2O_3/C exhibits different in action toward electrocatalytic activity, CV loop, onset potential as well as peak potential. The ORR kinetics is further investigated by RDE measurements. Figure 5.5. b presents the LSV curves portraying the current densities and onset potentials for the investigated ECs at 1600 rpm measured in O_2 saturated 0.1 M KOH solution. The trends in the ORR activity of the ECs are consistent with the results of the CV study. It is noteworthy that the weak electrocatalytic ORR performances exhibited by C have significantly enhanced on the introduction of Fe_2O_3 in terms of onset potential and current density. While Fe_2O_3-CeO_2/C shows more positive onset potential (0.81V) and half-wave potential ($E_{1/2}$ = 0.57 V) which is significantly higher than that of C, Fe_2O_3/C and CeO_2/C signifying a promotional effect after the CeO_2 modification.

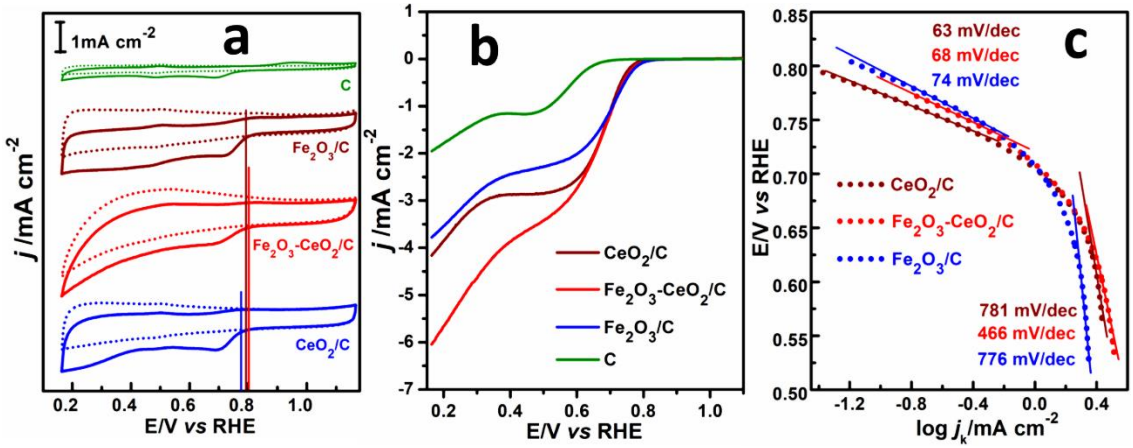

Figure 5.5. a) CVs of C, Fe_2O_3/C, Fe_2O_3-CeO_2/C and CeO_2/C in N_2 (dash-dotted lines) and O_2 (solid lines) saturated 0.1 M KOH solution. b) ORR LSV curves of C, Fe_2O_3/C, Fe_2O_3-CeO_2/C and CeO_2/C at 1600 rpm. c) Tafel plots of the ECs.

The limiting current density of Fe_2O_3-CeO_2/C at 1600 rpm is –6.05 mA cm^{-2} which is higher than that of CeO_2/C (–4.14 mA cm^{-2}), Fe_2O_3/C (–3.8 mA cm^{-2}), C (–1.9 mA cm^{-2}) and commercial Pt/C (–5.2 mA cm^{-2}). To evaluate the ORR kinetics, the corresponding Tafel plots are obtained from the ORR LSV curves. Figure 5.5. c presents the Tafel slopes for the investigated ECs calculated at both low overpotential and high overpotential regions. The Tafel slope of Fe_2O_3/C, Fe_2O_3-CeO_2/C and CeO_2/C are 74, 68 and 63 mV/dec, respectively while in the high overpotential region it is 776, 466 and 781 mV/dec, respectively. The lower Tafel slope of Fe_2O_3-CeO_2/C over a wide potential range is significant for the superior ORR. Fe_2O_3-CeO_2/C exhibit a considerably lower Tafel slope than that of the Fe_2O_3/C, which is due to the CeO_2 incorporation into the Fe_2O_3-CeO_2/C signifying faster kinetics for ORR.

To further investigate the ORR pathways and the kinetics catalyzed by the prepared ECs, RDE measurements at various rotations were performed. Figure 5.6. (a-c) presents the LSV polarization curves measured at different rotations in O_2-saturated 0.1 M KOH solution. The trends in the electrocatalytic activity of the ECs are comparable to those found in the CV study. Based on the LSV polarization curves the number of electrons (n) transferred during an elementary ORR process is calculated using Koutecky−Levich (K−L) equation [24]. K-L plots of the investigated ECs at

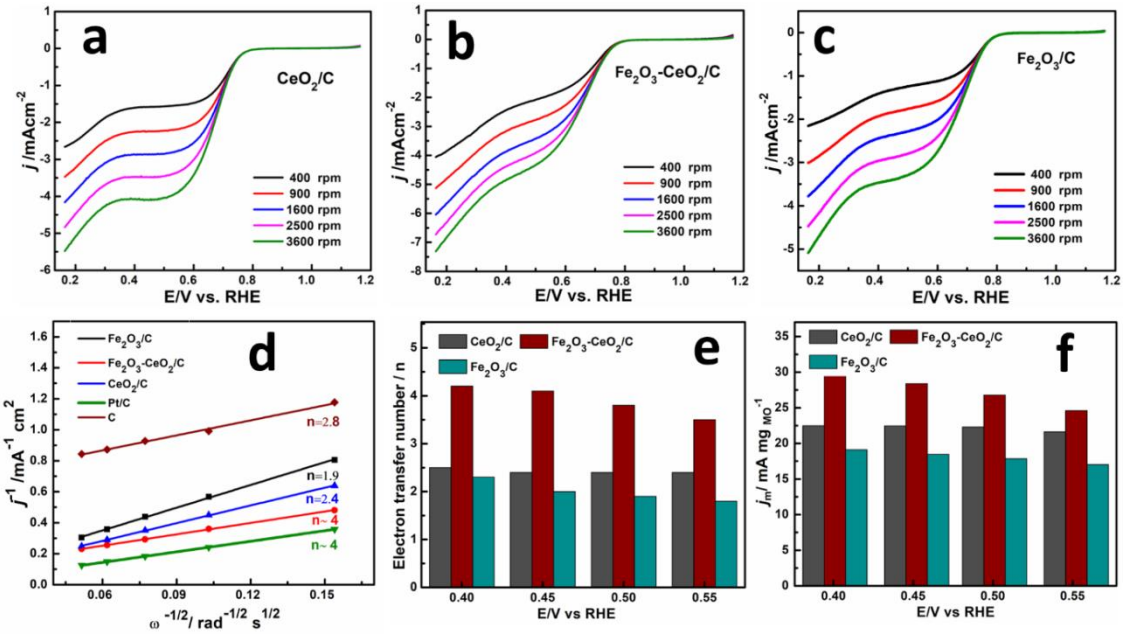

Figure 5.6. ORR polarization curves of a) CeO_2/C, b) Fe_2O_3-CeO_2/C, c) Fe_2O_3/C and d) K-L plots of Fe_2O_3/C, Fe_2O_3-CeO_2/C, CeO_2/C, Pt/C and C derived from the LSV polarization curves at 0.50 V, e) number of electrons transferred at various potentials and f) mass-specific activity (MA) of the as-prepared ECs.

0.50 V is shown in Figure 5.6. d which shows the 'n' values for Fe_2O_3/C, Fe_2O_3-CeO_2/C, Pt/C and C are 1.9, 4, 2.4, 4 and 2.8, respectively. Both the Fe_2O_3-CeO_2/C and Pt/C exhibit the $4e^-$ ORR process without forming H_2O_2 as an intermediate product. The linearity and parallel fitting lines of the K–L plots suggest first-order kinetics of the ORR catalysis. The $4e^-$ pathway is evaluated for the ECs over a wide potential range as shown in Figure 5.6. d which reveals that Fe_2O_3-CeO_2/C follows approximately $4e^-$ pathway over a wide range of potentials. Mass activity (MA) at 1600 rpm over the potential range of 0.40-0.55 V shows the ORR activity order of Fe_2O_3-CeO_2/C> CeO_2/C> Fe_2O_3/C for the set of investigated ECs (Figure 5.6. f) which describes the typical intrinsic electrocatalytic activity of the ECs.

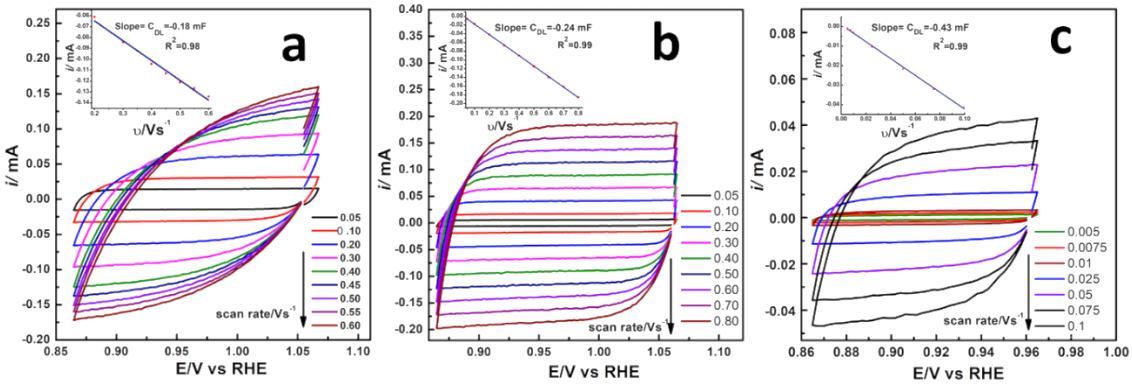

Figure 5.7. C_{dl} measurements for determining ECSA in 0.1 M KOH. a-c) represent CVs of Fe_2O_3/C, Fe_2O_3-CeO_2/C and CeO_2/C, respectively at various scan rates (insets show the corresponding slope obtained from respective CV data).

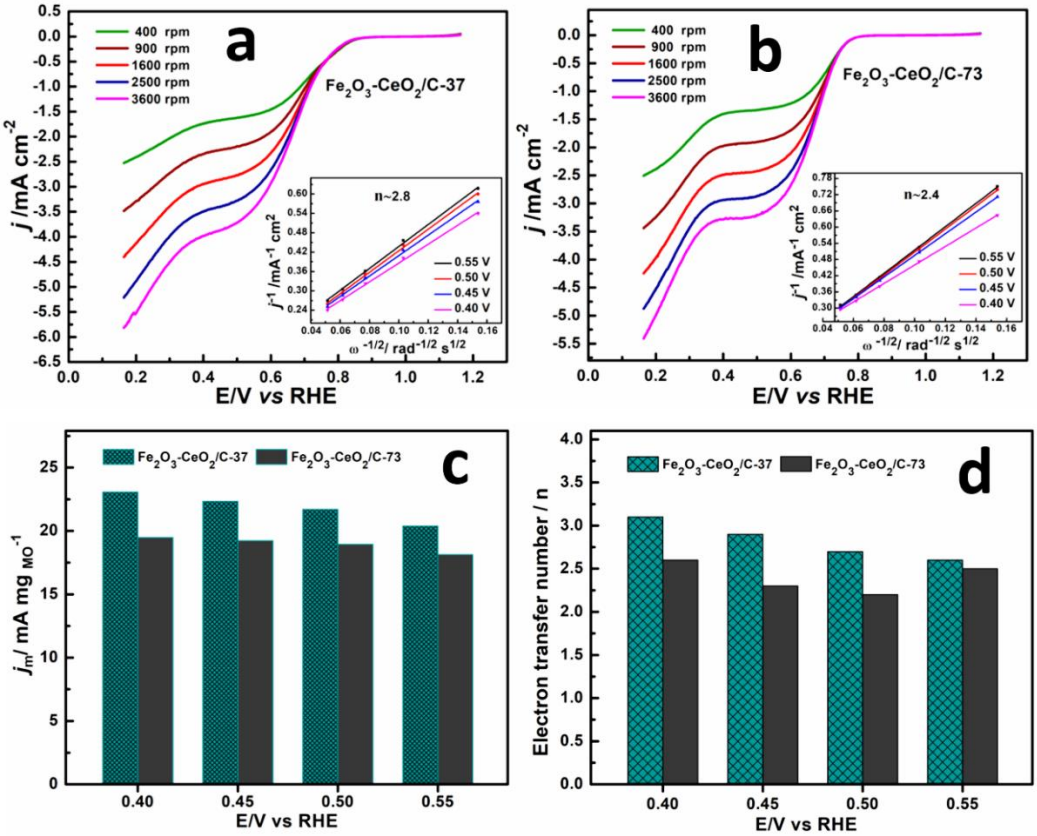

Figure 5.8. ORR polarization curves of a) Fe_2O_3-CeO_2/C-37, b) Fe_2O_3-CeO_2/C-73, c) mass-specific activity (MA) and d) number of electrons transferred at various potentials evaluated for Fe_2O_3-CeO_2/C-37 and Fe_2O_3-CeO_2/C-73.

The optimized Fe_2O_3 loading in the mixed catalyst is significant for the efficient ORR. The excessive or insufficient Fe_2O_3 in Fe_2O_3-CeO_2/C may decrease the ORR performance due to the lower intrinsic catalytic activity of Fe_2O_3 in contrast to CeO_2/C. Therefore, to study the effect of CeO_2 loading in Fe_2O_3-CeO_2/C on the ORR, we performed the activity measurement of Fe_2O_3-CeO_2/C-37 and Fe_2O_3-CeO_2/C-73. Figure 5.8. (a-d) show the ORR activities (LSV polarization curves, MA, and 'n' values) exhibited by Fe_2O_3-CeO_2/C-37 and Fe_2O_3-CeO_2/C-73. It is observed that the ORR performances are significantly reduced for both the ECs in comparison to Fe_2O_3-CeO_2/C. Thus, the comprehensive evaluation suggests that an equimolar Fe_2O_3-CeO_2 is essentially required for sustaining the synergy that can enhance the ORR process.

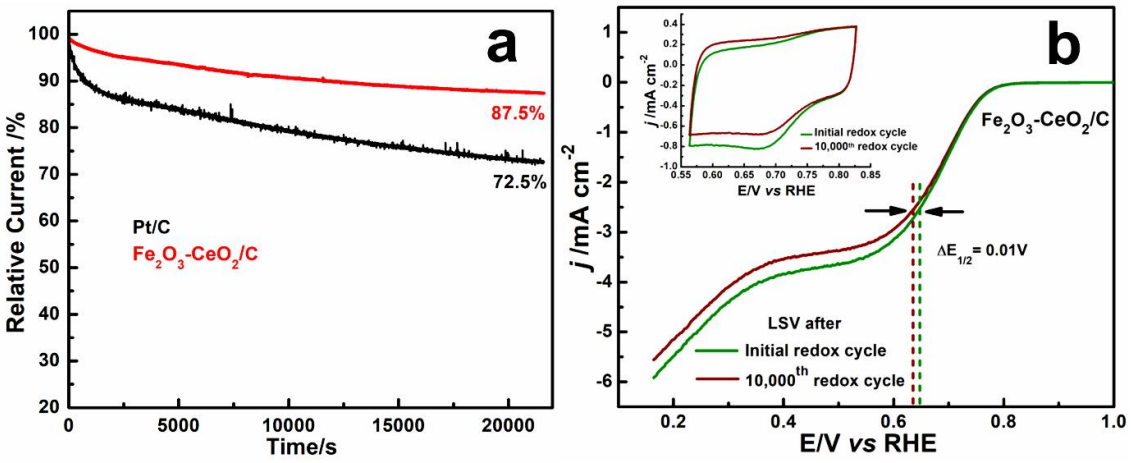

Figure 5.9. a) chronoamperometric test for Fe_2O_3-CeO_2/C and Pt/C, b) accelerated durability test (ADT) for Fe_2O_3-CeO_2/C.

The chronoamperometric test (Figure 5.9 a) displays the stability of Fe_2O_3-CeO_2/C with % degradation of current measured up to 6 h. Pt/C shows 72.5% of current while Fe_2O_3-CeO_2/C shows higher retention of current (87.5%) after 6 h. The accelerated durability test (ADT) performed up to 10000 redox cycles (Figure 5.9. b) reveals an outstanding current density with significantly smaller Δj of 0.04 mA cm^{-2} and $\Delta E_{1/2}$ of 0.01 V suggesting superior durability possessed by Fe_2O_3-CeO_2/C.

Table 5.2. Comparison of ORR activity of Fe_2O_3-CeO_2/C with analogous reported catalysts.*

Electrocatalysts	Electrolyte (KOH)	$E_{1/2}$ (V)	E_{onset} (V)	j (mA cm^{-2})	Tafel slope (mV dec^{-1})	Ref.
CuO_x−CeO_2/C	0.1 M	0.67	0.87	−5.03	65	[2]
α-MnO_2/Mn_3O_4/CeO_2/C	0.1 M	0.74	0.84	−6.63	--	[8]
MnO_x–CeO_2/KB	0.1 M	0.81	0.94	~ −5.10	94.4	[11]
Co_3O_4–CeO_2/KB	0.1 M	0.83	0.94	−5.35	83.9	[12]
Fe-Co_1.5/N,S-MPC	0.1 M	0.76	0.86	--	--	[25]
rGO/γ-Fe_2O_3	0.1 M	--	0.81	--	--	[26]
FePc/N-GP950	0.1 M	0.89	0.97	--	--	[27]
CeO_2-hG	0.1 M	0.79	0.90	--	58	[28]
Ag–CeO_2	0.1 M	0.72	0.91	--	96	[29]
5% Mn-CeO_2/rGO	0.1 M	0.63	0.83	−4.83	--	[30]
Fe2O3-CeO2/C	0.1 M	0.57	0.81	– 6.05	68	This work

*The potentials in a Ag/AgCl electrode were presented with respect to the RHE using the relation: $E_{RHE} = E_{Ag/AgCl} + E^o_{Ag/AgCl} + 0.059$ pH (considering a pH of 0.1 M KOH = 13), where E_{RHE} is the reversible hydrogen electrode potential, $E_{Ag/AgCl}$ is Ag/AgCl electrode potential and $E^o_{Ag/AgCl} = 0.1976$ at 25 °C.

Table 5.2 shows a comparative analysis of the ORR performances with some established MO-based ECs. The ORR activity exhibited by Fe_2O_3-CeO_2/C is superior in terms of current density and Tafel slope. It shows significant E_{onset} and $E_{1/2}$ which are comparable with the reported ECs. The fundamental cause for the superior ORR activity of Fe_2O_3-CeO_2/C is due to efficient charge transport and synergistic properties of the EC resulting in a favourable reduction of O_2. Vulcan carbon has several sp^2-C which provide a superior charge transfer rate. Adequate diffusion of molecular O_2 into the activated surface of the EC is one of the major factors for efficient electrocatalysis. CeO_2 with its characteristic redox properties unveiled rich oxygen vacancies resulting in enhanced O_2 transport, storage, and release through the Fe_2O_3-CeO_2 interfaces.

Thus, when the O_2 density gets lower at the high-current density, the adsorbed oxygen (O^*_{ad}) on CeO_2 cites accepts e^- facilitating the activation of O_2 and forming HO_2^-, followed by transfer to the proximate Fe_2O_3 active sites.

5.3. Conclusions

Fe_2O_3-CeO_2/C EC with a rich oxide-oxide interfacial structure was designed. The composite material unveils a high surface area including significant oxygen vacancy that could be beneficial for ORR. Fe_2O_3-CeO_2/C shows better kinetics with a smaller Tafel slope and higher MA accompanied by the highly anticipated $4e^-$ ORR process. Moreover, it offers an enhanced current density (– 6.05 mA cm^{-2}) steered by improved stability and high durability in contrast to that of Pt/C. Benefiting from the CeO_2-assisted oxygen vacancies, high BET surface area and strong oxide-oxide/C interface interactions, the Fe_2O_3-CeO_2/C composite enriches its synergistic mechanism toward a superior ORR, which establishes a promising method of designing highly active non-precious MO-based EC for future green energy production.

References

[1] Seh, Z. W., Kibsgaard, J., Dickens, C. F., Chorkendorff, I. B., Nørskov, J. K., and Jaramillo, T. F. Combining theory and experiment in electrocatalysis: Insights into materials design. *Science*, 355(6321): eaad4998, 2017.

[2] Goswami, C., Yamada, Y., Matus, E. V., Ismagilov, I. Z., Kerzhentsev, M., and Bharali, P. Elucidating the role of oxide–oxide/carbon interfaces of CuO_x–CeO_2/C in boosting electrocatalytic performance. *Langmuir*, 36(49):15141-15152, 2020.

[3] Qi, W., Yi, W., Jiang, W., Ling, R., Yang, C., Liu, S., Jun, S.C., Yamauchi, Y. and Cao, B., Interfacial assembled CeO_{2-x}/Co@ N-doped carbon hollow nanohybrids for high-performance lithium–sulfur batteries. *ACS Sustainable Chemistry & Engineering*, 9(43):14451-14460, 2021.

[4] Sahoo, L., and Gautam, U. K. Boosting bifunctional oxygen reduction and methanol oxidation electrocatalytic activity with 2D superlattice-forming Pd nanocubes generated by precise acid etching. *ACS Applied Nano Materials*, 3(8):8117-8125, 2020.

[5] Li, Y., Li, Q., Wang, H., Zhang, L., Wilkinson, D. P., and Zhang, J. Recent progresses in oxygen reduction reaction electrocatalysts for electrochemical energy applications. *Electrochemical Energy Reviews*, 2(4):518-538, 2019.

[6] Srivastava, R., Mani, P., Hahn, N., and Strasser, P. Efficient oxygen reduction fuel cell electrocatalysis on voltammetrically dealloyed Pt–Cu–Co nanoparticles. *Angewandte Chemie International Edition*, 46(47):8988-8991, 2007.

[7] Morozan, A., Jousselme, B., and Palacin, S. Low-platinum and platinum-free catalysts for the oxygen reduction reaction at fuel cell cathodes. *Energy & Environmental Science*, 4(4):1238-1254, 2011.

[8] Chutia, B., Hussain, N., Puzari, P., Jampaiah, D., Bhargava, S. K., Matus, E. V., Ismagilov, I.Z., Kerzhentsev, M. and Bharali, P., Unraveling the role of CeO_2 in stabilization of multivalent Mn species on α-MnO_2/Mn_3O_4/CeO_2/C surface for enhanced electrocatalysis. *Energy & Fuels*, 35(13):10756-10769, 2021.

[9] Sun, M., Zhang, G., Liu, H., Liu, Y., and Li, J., α-and γ-Fe_2O_3 nanoparticle/nitrogen doped carbon nanotube catalysts for high-performance oxygen reduction reaction. *Science China Materials*, 58(9):683-692, 2015.

[10] Hazarika, K. K., Goswami, C., Saikia, H., Borah, B. J., and Bharali, P. Cubic Mn_2O_3 nanoparticles on carbon as bifunctional electrocatalyst for oxygen reduction and oxygen evolution reactions. *Molecular Catalysis*, 451:153-160, 2018.

[11] Chen, J., Zhou, N., Wang, H., Peng, Z., Li, H., Tang, Y., nad Liu, K. Synergistically enhanced oxygen reduction activity of MnO_x–CeO_2/Ketjenblack composites. *Chemical Communications*, 51(50):10123-10126, 2015.

[12] Liu, K., Huang, X., Wang, H., Li, F., Tang, Y., Li, J., and Shao, M. Co_3O_4–CeO_2/C as a highly active electrocatalyst for oxygen reduction reaction in Al–air batteries. *ACS Applied Materials & Interfaces*, 8(50):34422-34430, 2016.

[13] Saikia, H., Hazarika, K. K., Chutia, B., Choudhury, B., and Bharali, P. A simple chemical route toward high surface area CeO_2 nanoparticles displaying remarkable radical scavenging activity. *ChemistrySelect*, 2(11):3369-3375, 2017.

[14] Huang, M., Yao, Q., Feng, G., Zou, H., and Lu, Z. H. Nickel–ceria nanowires embedded in microporous silica: controllable synthesis, formation mechanism, and catalytic applications. *Inorganic Chemistry*, 59(8):5781-5790, 2020.

[15] Lee, J. S., Park, G. S., Lee, H. I., Kim, S. T., Cao, R., Liu, M., and Cho, J. Ketjenblack carbon supported amorphous manganese oxides nanowires as highly efficient electrocatalyst for oxygen reduction reaction in alkaline solutions. *Nano Letters*, 11(12):5362-5366, 2011.

[16] Jampaiah, D., Velisoju, V. K., Devaiah, D., Singh, M., Mayes, E. L., Coyle, V. E., Reddy, B.M., Bansal, V. and Bhargava, S.K., Flower-like Mn_3O_4/CeO_2 microspheres as an efficient catalyst for diesel soot and CO oxidation: synergistic effects for enhanced catalytic performance. *Applied Surface Science*, 473:209-221, 2019.

[17] Arani, H. F., Mirhabibi, A. R., Collins, S., Daroughegi, R., Soltani, A. K., Naghizadeh, R., Riahi-Noori, N., Aghababazadeh, R. and Westwood, A., Enhancement in graphitization of coal tar pitch by functionalized carbon nanotubes. *RSC Advances*, *7*(9):5533-5540, 2017.

[18] Garcia, D., Picasso, G., Hidalgo, P., Peres, H. E., Kou, R. S., and Gonçalves, J. M. Sensors based on Ag-loaded hematite (α-Fe_2O_3) nanoparticles for methyl mercaptan detection at room temperature. *Analytical Chemistry Research*, 12:74-81, 2017.

[19] JMcBride, J. R., Hass, K. C., Poindexter, B. D., and Weber, W. H. Raman and x-ray studies of $Ce_{1-x}RE_xO_{2-y}$, where RE= La, Pr, Nd, Eu, Gd, and Tb. *Journal of Applied Physics*, 76(4):2435-2441, 1994.

[20] Qiu, F., Shi, J., Guo, M., Chen, S., Xia, J., and Lu, Z. H. Rapid synthesis of large-size Fe_2O_3 nanoparticle decorated NiO nanosheets via electrochemical exfoliation for enhanced oxygen evolution electrocatalysis. *Inorganic Chemistry*, 60(2):959-966, 2020.

[21] Nguyen, T. D., Dinh, C. T., and Do, T. O. Monodisperse samarium and cerium orthovanadate nanocrystals and metal oxidation states on the nanocrystal surface. *Langmuir*, 25(18):11142-11148, 2009.

[22] Zhang, Z., Luo, Y., Liu, S., Yao, Q., Qing, S., and Lu, Z. H. A PdAg-CeO_2 nanocomposite anchored on mesoporous carbon: a highly efficient catalyst for hydrogen production from formic acid at room temperature. *Journal of Materials Chemistry A*, 7(37):21438-21446, 2019.

[23] Wang, Z., Wang, W., Zhang, L., and Jiang, D. Surface oxygen vacancies on Co_3O_4 mediated catalytic formaldehyde oxidation at room temperature. *Catalysis*

Science & Technology, 6(11):3845-3853, 2016.

[24] Liu, R., Wu, D., Feng, X., and Müllen, K. Nitrogen-doped ordered mesoporous graphitic arrays with high electrocatalytic activity for oxygen reduction. *Angewandte Chemie International Edition*, 49(14):2565-2569, 2010.

[25] Kostuch, A., Gryboś, J., Wierzbicki, S., Sojka, Z., and Kruczała, K. Selectivity of mixed iron-cobalt spinels deposited on a N, S-doped mesoporous carbon support in the oxygen reduction reaction in alkaline media. *Materials*, 14(4):820, 2021.

[26] Karunagaran, R., Coghlan, C., Tung, T. T., Kabiri, S., Tran, D. N., Doonan, C. J., and Losic, D. Study of iron oxide nanoparticle phases in graphene aerogels for oxygen reduction reaction. *New Journal of Chemistry*, 41(24):15180-15186, 2017.

[27] Park, J. S., and Chang, D. W. Iron phthalocyanine/graphene composites as promising electrocatalysts for the oxygen reduction reaction. *Energies*, 13(16):4073, 2020.

[28] Grewal, S., Macedo Andrade, A., Liu, Z., Garrido Torres, J. A., Nelson, A. J., Kulkarni, A., Bajdich, M. and Lee, M.H. Highly active bifunctional oxygen electrocatalytic sites realized in ceria–functionalized graphene. *Advanced Sustainable Systems*, 4(8):2000048, 2020.

[29] Sun, S., Xue, Y., Wang, Q., Li, S., Huang, H., Miao, H., and Liu, Z. Electrocatalytic activity of silver decorated ceria microspheres for the oxygen reduction reaction and their application in aluminium–air batteries. *Chemical Communications*, *53*(56):7921-7924, 2017.

[30] Hota, I., Soren, S., Mohapatra, B. D., Debnath, A. K., Muthe, K. P., Varadwaj, K. S. K., and Parhi, P. Mn-doped ceria/reduced graphene oxide nanocomposite as an efficient oxygen reduction reaction catalyst. *Journal of Electroanalytical Chemistry*, 851:113480, 2019.